ceramics

MDPI

Article

Characterization of Bipolar Transport in $Hf(Te_{1-x}Se_x)_2$ Thermoelectric Alloys

Seong-Mee Hwang †, Sang-il Kim †, Jeong-Yeon Kim, Minsu Heo and Hyun-Sik Kim *

Department of Materials Science and Engineering, University of Seoul, 163 Seoulsiripdae-ro, Dongdaemun-gu, Seoul 02504, Republic of Korea

* Correspondence: hyunsik.kim@uos.ac.kr

† These authors contributed equally to this work.

Abstract: Control of bipolar conduction is essential to improve the high-temperature thermoelectric performance of materials for power generation applications. Recently, $Hf(Te_{1-x}Se_x)_2$ alloys have gained much attention due to their potential use in thermoelectric power generation. Increasing the Se alloying content significantly increases the band gap while decreasing its carrier concentration. These two factors affect bipolar conduction substantially. In addition, the weighted mobility ratio is estimated from the experimental electronic transport properties of $Hf(Te_{1-x}Se_x)_2$ alloys (x = 0.0, 0.025, 0.25, 0.5, 1.0) by using the Two-Band model. From the bipolar thermal conductivity also calculated using the Two-Band model, we find that it peaks near x = 0.5. The initial bipolar conductivity increase of $x < 0.5$ is mostly due to the decrease in the weighted mobility ratio and carrier concentration with increasing x. For $x > 0.5$, the drop in the bipolar conductivity can be understood with significant band gap enlargement.

Keywords: $Hf(Te_{1-x}Se_x)_2$; bipolar thermal conductivity; weighted mobility ratio; Two-Band model; band gap

check for updates

Citation: Hwang, S.-M.; Kim, S.-i.; Kim, J.-Y.; Heo, M.; Kim, H.-S. Characterization of Bipolar Transport in $Hf(Te_{1-x}Se_x)_2$ Thermoelectric Alloys. *Ceramics* **2023**, *6*, 538–547. https://doi.org/10.3390/ceramics6010032

Academic Editor: Yung C. Shin

Received: 27 December 2022
Revised: 1 February 2023
Accepted: 14 February 2023
Published: 17 February 2023

1. Introduction

Thermoelectric technology can be used to harvest electricity from waste heat. Because the burning of no fossil fuels is required to produce electricity, the demand for thermoelectric technology is growing fast. The process of generating electricity using the thermoelectric device is also simple. When one side of the thermoelectric device (p- and n-type thermoelectric elements connected in series) is attached to the waste heat source, the induced temperature gradient across the device makes holes (in the p-type element) and electrons (in the n-type element) move away from the heat source while generating electricity [1–5]. The conversion (from heat to electricity) efficiency of the thermoelectric device is largely determined by the thermoelectric performance of the materials used in the device. Most importantly, how much electric voltage is induced within the thermoelectric material due to the applied temperature gradient is defined as the Seebeck coefficient (S). To achieve high conversion efficiency in the thermoelectric device, thermoelectric materials with high S is desired. However, the thermoelectric performance of a material is better represented by a Figure-of-merit zT than the S alone. The zT is defined as Equation (1) [6].

$$zT = \frac{S^2 \sigma T}{\kappa_e + \kappa_l} \quad (1)$$

The σ, κ_e, κ_l, and T are the electrical conductivity, thermal conductivity by charged carriers, lattice thermal conductivity, and temperature (unit of K), respectively. According to Equation (1), the S and σ (electronic properties) need to be improved while suppressing κ_e and κ_l (thermal properties) to enhance zT. The thermoelectric parameters in Equation (1) are interconnected with one another, except κ_l. If the σ is increased by increasing the Hall

carrier concentration (n_H), the S will decrease but κ_e will increase. For this reason, the zT is always optimized at a narrow range of n_H. To avoid any complication, many researchers have focused on reducing κ_l or the engineering band structure to overcome the strong S–σ trade-off relation [7–13]. The strong S–σ trade-off relation observed in thermoelectric materials is mainly due to the density-of-states effective mass (m_d*) of the material. At a fixed carrier concentration, increasing m_d* increases the S while decreasing the σ. However, more specifically, the S is related to the m_d*, but the σ is related to the single band mass (m_b) and not to the m_d* directly. Of course, the m_d* is a product of m_b and the number of valley degeneracy to the power of 2/3 ($N_V{}^{2/3}$). If we can increase the S without decreasing σ, the strong S–σ trade-off relationship can be overcome. It can be achieved if the increase in S is due to N_V increase and not the m_b increase. The improvement of S via the N_V increase can be achieved by converging adjacent bands, and in this case, σ will remain intact.

As one of the approaches to bypass the S–σ trade-off relationship, semiconducting transition metal dichalcogenides (TMDs) have been studied extensively because of their novel electronic and thermal properties [14–20]. According to Yumnam et al., HfX_2 (X = S, Se) compounds exhibit high theoretical S and σ at the same time, stemming from the interaction between the light and heavy bands. In addition, they show significantly low theoretical κ_l (< 2 W m^{-1} K^{-1}) due to the low phonon group velocity [21]. Recently, Bang et al. have reported experimental electronic transport properties of bulk $Hf(Te_{1-x}Se_x)_2$ alloys (x = 0.0–1.0). A high-power factor ($PF = S^2\sigma$) of 0.24 mW m^{-1} K^{-1} is obtained for $HfTe_2$ at 600 K [22]. They also provide how band parameters such as the m_d*, non-degenerate mobility (μ_0), and weighted mobility (μ_W) change as the Se alloying content increases from 0.0 ($HfTe_2$) to 1.0 ($HfSe_2$) using the Single Parabolic Band (SPB) model [23]. Based on the SPB model, increasing the Se alloying content sharply decreases m_d*, μ_0, and μ_W. Bang et al. also report that the band gap estimated by using the Goldsmid–Sharp equation increases significantly with the increasing Se alloying content [24,25]. However, the effect of the band gap increase was not taken into consideration when estimating the electronic band parameters.

Here, the effect of the band gap change in the electronic transport properties of bulk $Hf(Te_{1-x}Se_x)_2$ alloys (x = 0.0, 0.025, 0.25, 0.5, and 1.0) is investigated using the Two-Band (TB) model. Experimental n_H-dependent S and Hall mobility (μ_H) are used to estimate $m_{d,i}$*, $\mu_{0,i}$, and $\mu_{W,i}$ (i = *maj* for majority carrier band and *min* for minority carrier band) for one valence band and one conduction band that contribute to electronic transport. From the individual band parameter for each band, the ratio of majority carrier-weighted mobility to minority carrier-weighted mobility, A, and bipolar thermal conductivity (κ_b) are also characterized. The calculated κ_b at 300 K peaks when x = 0.5, and this is an interplay among A, the Goldsmid–Sharp band gap ($E_{g,G\text{-}S}$), and n_H that are known to affect the κ_b, but change differently with increasing x.

2. Materials and Methods

The ingots of $Hf(Te_{1-x}Se_x)_2$ (x = 0, 0.025, 0.25, 0.5, and 1) were first prepared using melting stoichiometrically weighed Hf (99.6%), Te (99.999%), and Se (99.999%) powders within vacuum quartz tubes at 950 °C for 60 h. The ingots were transferred to a glove box and pulverized in the glove box into powders using a mortar and pestle. The powders were then sintered using a spark plasma sintering at 580 °C for 10 min under 50 MPa in a vacuum. The Hall carrier concentration and Hall mobility of the sintered samples were obtained from the Hall coefficient measured via the Van der Pauw method using a commercial Hall measurement system (AHT-55T5 from Ecopia, Anyang, South Korea) under a magnetic field of 0.5 T. For the samples with low Hall mobility, a very thin sample (~ 500 μm) is fabricated to minimize measurement errors.

The $m_{d,i}$* and $\mu_{0,i}$ (i = *maj*, *min*) are fitted to the experimental n_H-dependent S and σ, respectively, using the TB model. According to the TB model, the S_i, σ_i, and Hall coefficient ($R_{H,i}$) (i = *maj*, *min*) are defined as below.

$$S_{maj} = \frac{k_B}{e}\left(\frac{2F_1(\eta)}{F_0(\eta)} - \eta\right) \tag{2}$$

$$S_{min} = \frac{k_B}{e}\left(\frac{2F_1(-\eta-\varepsilon_g)}{F_0(-\eta-\varepsilon_g)} + \eta + \varepsilon_g\right) \tag{3}$$

$$S = \frac{S_{maj}\sigma_{maj} + S_{min}\sigma_{min}}{\sigma_{maj} + \sigma_{min}} \tag{4}$$

$$\sigma_{maj} = \left(\frac{e^3h^5}{48\sqrt{2}\pi^5}\right)\frac{\mu_{0,maj}}{\left(m^*_{d,maj}k_BT\right)^{3/2}}F_0(\eta) \tag{5}$$

$$\sigma_{min} = \left(\frac{e^3h^5}{48\sqrt{2}\pi^5}\right)\frac{\mu_{0,min}}{\left(m^*_{d,min}k_BT\right)^{3/2}}F_0(-\eta-\varepsilon_g) \tag{6}$$

$$\sigma = \sigma_{maj} + \sigma_{min} \tag{7}$$

$$\frac{1}{R_{H,maj}} = \frac{16\pi e}{3}\left(\frac{2m^*_{d,maj}k_BT}{h^2}\right)^{3/2}\frac{(F_0(\eta))^2}{F_{-1/2}(\eta)} \tag{8}$$

$$\frac{1}{R_{H,min}} = \frac{16\pi e}{3}\left(\frac{2m^*_{d,min}k_BT}{h^2}\right)^{3/2}\frac{(F_0(-\eta-\varepsilon_g))^2}{F_{-1/2}(-\eta-\varepsilon_g)} \tag{9}$$

$$R_H = \frac{R_{H,maj}\sigma^2_{maj} + R_{H,min}\sigma^2_{min}}{(\sigma_{maj}+\sigma_{min})^2} \tag{10}$$

$$n_H = \frac{1}{R_He} \tag{11}$$

The k_B, e, η, h, ε_g, and F_j are the Boltzmann constant, electric charge, fermi level, Planck constant, band gap divided by k_BT, and Fermi integral of order j (Equation (12)).

$$F_j(\eta) = \int_0^\infty \frac{\varepsilon^j}{1+\exp(\varepsilon-\eta)}d\varepsilon \tag{12}$$

The calculated S (Equation (4)) as a function of n_H (Equation (11)) is fitted to the measurement to obtain $m_{d,i}$* (i = *maj*, *min*). The calculated σ (Equation (7)) as a function of n_H (Equation (11)) is fitted to the measurement to obtain $\mu_{0,i}$ (i = *maj*, *min*). The ε_g for $Hf(Te_{1-x}Se_x)_2$ (x = 0.0, 0.025, 0.25, 0.5, and 1.0) are adopted from Bang et al. and they are listed in the Table 1 below [22]. In a Single Parabolic Band (SPB) model, where we assume there is only one band participating in the electronic transport properties, we only have to fit one band parameter, which is the m_d* to the experimental n_H-dependent S. However, in the TB model, the total S is an electrical conductivity-weighted average between S_{maj} and S_{min} (Equation (4)). In other words, when there are two bands participating in transport, even when we want to describe the experimental n_H-dependent S, both $m_{d,i}$* (i = *maj*, *min*) and $\mu_{0,i}$ (i = *maj*, *min*) need to be fitted simultaneously while changing the ε_g for different x. Therefore, instead of fitting m_d* from the n_H-dependent S and μ_0 from the n_H-dependent σ, consecutively, all four unknown band parameters $m_{d,i}$* (i = *maj*, *min*) and $\mu_{0,i}$ (i = *maj*, *min*) were fitted to n_H-dependent S and σ concurrently. Plus, to minimize the complexity of the TB modeling, once the $m_{d,imin}$* and $\mu_{0,min}$ were fitted in x with the lowest ε_g (where the contribution from the minority carrier band is maximum), they were kept constant for

the TB model calculation of the samples with different x. This is because the impact of the minority carrier band on the electronic transport properties decreases with an increasing ε_g.

Table 1. The ε_g for $Hf(Te_{1-x}Se_x)_2$ (x = 0.0, 0.025, 0.25, 0.5, and 1.0) at 300 K [22].

x in $Hf(Te_{1-x}Se_x)_2$	ε_g (Band gap/k_BT)
0.0	2.06
0.025	2.19
0.25	3.12
0.5	5.92
1.0	20.00

The $\mu_{W,i}$ is characterized from the estimated $m_{d,i}$* and $\mu_{0,i}$ (i = *maj*, *min*) via Equation (13) (m_0 is the electron rest mass).

$$\mu_{W,i} = \mu_{0,i}\left(\frac{m^*_{d,i}}{m_0}\right)^{3/2} \tag{13}$$

The weighted mobility ratio a is computed using Equation (14).

$$A = \frac{\mu_{W,maj}}{\mu_{W,min}} \tag{14}$$

3. Results and Discussion

3.1. Estimation of the $m_{d,i}$ (i = VB, CB) Via the TB Model*

Figure 1a presents the experimental S in terms of n_H at 300 K adopted from Bang et al. (in symbols) [22]. The magnitude of S drastically increases with the increasing Se alloying content (x). While S of the samples with $x \leq 0.25$ is smaller than 30 μV K^{-1}, the S of x = 0.5 and x = 1.0 amount to 220 and 730 μV K^{-1}, respectively. On the contrary, measured n_H significantly decrease with increasing x. For example, the n_H of x = 0.0, which is 7.7 × 10^{20} cm^{-3}, sharply decreases to 3.0 × 10^{16} cm^{-3} when x = 1.0. If we assume that there is only one electronic band contributing to the electronic transport properties of the sample, the S increase with x would be explained by the fermi level (η) decrease with the increasing Se alloying content (x) (Equation (2)). The n_H depends both on η and m_d* (Equations (8) and (11)). Again, with a single band contributing to electronic transport, the n_H decrease with x can be explained with η and m_d*. Both η and m_d* are directly proportional to the n_H. Because we already know that the η decreases with x, the measured n_H decrease with x suggests that the m_d* can be decreased or increased with x. Here, the effect of m_d* increase in n_H should be smaller than the effect of η decrease in n_H.

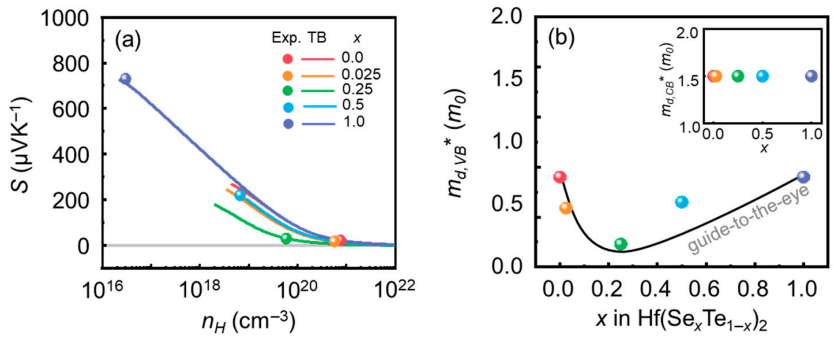

Figure 1. (**a**) Experimental (symbols) and theoretical (lines) S in terms of n_H for $Hf(Te_{1-x}Se_x)_2$ (x = 0.0, 0.025, 0.25, 0.5, and 1.0) at 300 K [22], (**b**) estimated $m_{d,VB}$* (=m_d* for holes) in terms of Se alloying content (x) at 300 K. The x-dependent $m_{d,CB}$* (=m_d* for electrons) at 300 K is provided in the inset.

However, when we take the minority carrier band into consideration as well to describe the experimental S in terms of n_H, we must consider how $\mu_{0,i}$ (i = *maj*, *min*) and ε_g change with x to estimate $m_{d,i}$* (i = *maj*, *min*) (Equations (2)–(4) and (8)–(11)). According to Table 1, the band gap increases significantly with x. In other words, the effect of the minority carrier band (conduction band in the case of $Hf(Te_{1-x}Se_x)_2$) in electronic transport decreases with x. The lines in Figure 1a are the TB model calculation results. From the fact that the lines in Figure 1a coincide with the experimental data in symbols, we can conclude that the fitted band parameters capture important features of the electronic bands in $Hf(Te_{1-x}Se_x)_2$. The reason that the TB model calculation results (in lines) are only available for $n_H > 10^{18}$ cm^{-3} for $x < 1.0$ is that for $n_H < 10^{18}$ cm^{-3}, the TB model results in a change in the type of material change due to the narrow band gap ($x < 1.0$).

Figure 1b shows the $m_{d,VB}$* (= $m_{d,maj}$*) and $m_{d,CB}$* (= $m_{d,min}$* in the inset) of $Hf(Te_{1-x}Se_x)_2$ (x = 0.0, 0.025, 0.25, 0.5, and 1.0) estimated by using the TB model at 300 K. To avoid any complexity, the $m_{d,CB}$* of $Hf(Te_{1-x}Se_x)_2$ was kept constant for all x (1.5 m_0). According to the TB model, the $m_{d,VB}$* first decreases with x and increases again after x = 0.25. For example, while the $m_{d,VB}$* at x = 0.0 and 1.0 are the same (0.9 m_0), that at x = 0.25 is the lowest (0.23 m_0). The gray solid line is also provided for the guide-to-the-eye. The Se alloying makes the $m_{d,VB}$* lighter until x = 0.25 and for x greater than 0.25, and the same Se alloying increases the $m_{d,VB}$*. The increase in $m_{d,VB}$* for $x \geq 0.25$ may have increased the corresponding n_H. However, the observed decrease in n_H with increasing x must be the η decrease that outweighs the $m_{d,VB}$* increase for $x \geq 0.25$.

3.2. Estimation of the $\mu_{0,i}$ (i = VB, CB) Via the TB Model

Figure 2a shows the experimental μ_H in terms of n_H at 300 K adopted from Bang et al. (in symbols) [22]. The μ_H is substantially suppressed with increasing x. The μ_H of approximately ~13 cm^2 V^{-1} s^{-1} for x = 0.0 and 0.025 is decreased down to 0.15 cm^2 V^{-1} s^{-1} when x = 1.0. Because only the x = 0.0 and 0.025 samples have n_H that are higher than 5×10^{20} cm^{-3} (other samples with $x \geq 0.25$ have n_H those are lower than 5×10^{19} cm^{-3}), only the x = 0.0 and 0.025 samples have σ that are higher than 1200 S cm^{-1} ($\sigma = e\ \mu_H\ n_H$). The σ of the samples with $x \geq 0.25$ are lower than 100 S cm^{-1} at 300 K [22]. In order to evaluate the characteristics of the electronic bands contributing to the electronic transport, we need to convert the μ_H into μ_0. The μ_H is a function of μ_0 and η, so depending on η, the trend observed in μ_H may not reflect the trend in the band parameter, μ_0, which represents the carrier mobility without any defects. By fitting $m_{d,i}$* and $\mu_{0,i}$ (i = *maj*, *min*) with different ε_g (Table 1) to the experimental μ_H in terms of n_H by using the TB model, the lines in Figure 2a that accurately describe the experimental data (in symbols) are obtained. From the reasonable agreements between the experiments and the TB model results, we demonstrate that the band parameter $\mu_{0,i}$ (i = *maj*, *min*) provided in Figure 2b describes the electronic bands well.

Figure 2b shows the $\mu_{0,VB}$ (=$\mu_{0,maj}$) and $\mu_{0,CB}$ (=$\mu_{0,min}$ in the inset) of $Hf(Te_{1-x}Se_x)_2$ (x = 0.0, 0.025, 0.25, 0.5, and 1.0) estimated by using the TB model at 300 K. Again, to minimize any complications, the $\mu_{0,CB}$ is kept constant for all different x (0.84 cm^2 V^{-1} s^{-1}). Overall, the $\mu_{0,VB}$ decreases with increasing x. At first, the μ_0,VB rapidly decreases with x, but for $x > 0.25$, the rate of the $\mu_{0,VB}$ decrease decreases. The guide-to-the-eye is provided in the gray solid line. This suggests that increasing the Se alloying content deteriorates the mobility of the holes. The physical reason behind the $\mu_{0,VB}$ reduction can be found by looking at how the carrier–phonon interaction changes with Se alloying. The μ_0 of any band is related to the m_d* and deformation potential (E_{def}), as in Equation (15). The $\hbar$ and C_l in Equation (15) are the $h/2\pi$ and the elastic constant, respectively.

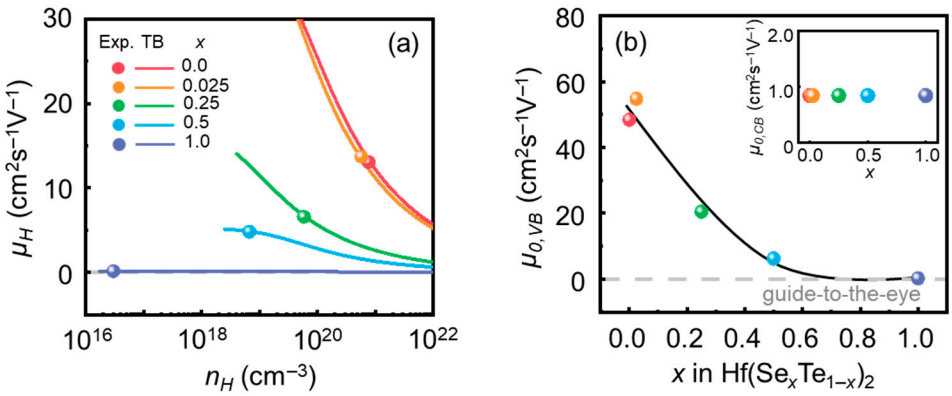

Figure 2. (**a**) Experimental (symbols) and theoretical (lines) μ_H in terms of n_H for Hf(Te$_{1-x}$Se$_x$)$_2$ (x = 0.0, 0.025, 0.25, 0.5, and 1.0) at 300 K [22], (**b**) estimated $\mu_{0,VB}$ (=μ_0 for holes) in terms of Se alloying content (x) at 300 K. The x-dependent $\mu_{0,CB}$ (=μ_0 for electrons) at 300 K is provided in the inset.

$$\mu_0 = \left(\frac{2\sqrt{2\pi}}{3}\right)\frac{e\hbar^4}{(k_B T)^{3/2}}\frac{C_l}{m_d^{*5/2}E_{def}^2} \tag{15}$$

As shown in Equation (15), the μ_0 is inversely proportional to $E_{def}{}^2$. The E_{def} quantifies how strong the scattering of charged carriers is due to lattice vibrations (phonons). If the E_{def} is high, this means that the charged carriers are more often scattered by phonons hindering the electronic transport properties. The $E_{def,VB}$ (the E_{def} of the valence band) for different x are obtained from $m_{d,VB}{}^*$ (Figure 1b) and $\mu_{0,VB}$ (Figure 2b), and are provided in Table 2. The general trend observed in $E_{def,VB}$ is that the carrier–phonon interaction becomes stronger as x increases. However, it is to be noted that there is a local minimum in $E_{def,VB}$ at x = 0.5.

Table 2. The $m_{d,VB}{}^*$, $\mu_{0,VB}$, and $E_{def,VB}$ for Hf(Te$_{1-x}$Se$_x$)$_2$ (x = 0.0, 0.025, 0.25, 0.5, and 1.0) at 300 K.

x in Hf(Te$_{1-x}$Se$_x$)$_2$	$m_{d,VB}{}^*$ (m_0)	$\mu_{0,VB}$ (cm^2 V^{-1} s^{-1})	$E_{def,VB}$ (eV)
0.0	0.9	48.39	0.051
0.025	0.59	54.78	0.081
0.25	0.23	20.45	0.43
0.5	0.65	6.19	0.21
1.0	0.9	0.17	0.86

3.3. Estimation of the $\mu_{W,i}$ (i = VB, CB) Via the TB Model

Figure 3a shows the experimental power factor (= $S^2\sigma$, PF) in terms of n_H at 300 K adopted from Bang et al. (in symbols) [22]. The experimental PF decreases significantly with increasing x, except when x = 0.5. When x = 0.5 (PF = 0.025 mW m^{-1} K^2), the corresponding PF is approximately four times greater than that measured when x = 0.25 (PF = 0.006 mW m^{-1} K^2). However, when x = 1.0, its PF decreases to lower than 0.001 mW m^{-1} K^2. According to Figure 1a, the S of x = 1.0 (S = 730 μV K^{-1}) is much higher than those of other x. However, the μ_H of x = 1.0 is the lowest mostly due to high E_{def} (Table 2). The PF is a product between S^2 and σ (= $e\ \mu_H\ n_H$). The large PF discrepancy between x = 0.0 and 1.0 is mostly due to the significant difference in n_H (incorporated in σ). While the n_H of x = 0.0 is in the order of 10^{21} cm^{-3}, that for x = 1.0 is only in the order of 10^{16} cm^{-3}. The factor of 10^5 difference cannot be offset, even with a large difference in the S. Based on the $m_{d,i}{}^*$ and $\mu_{0,i}$ (i = VB, CB) estimated using the TB model (Figures 1b and 2b), the PF in terms of n_H are estimated for different x (Figure 3a in lines). Regardless of the x, the theoretical maximum PF are predicted near 10^{19} cm^{-3}, and the predicted maximum

PF decreases significantly with increasing x. The theoretical maximum *PF* for $x = 0.0$ is as high as 0.37 mW $m^{-1}K^2$. Since the experimental *PF* for $x = 0.0$ is only 0.076 mW m^{-1} K^2, when the n_H is tuned from 7.7×10^{20} to 2.8×10^{20} cm^{-3}, an improvement of approximately 4.5 times in the *PF* is expected.

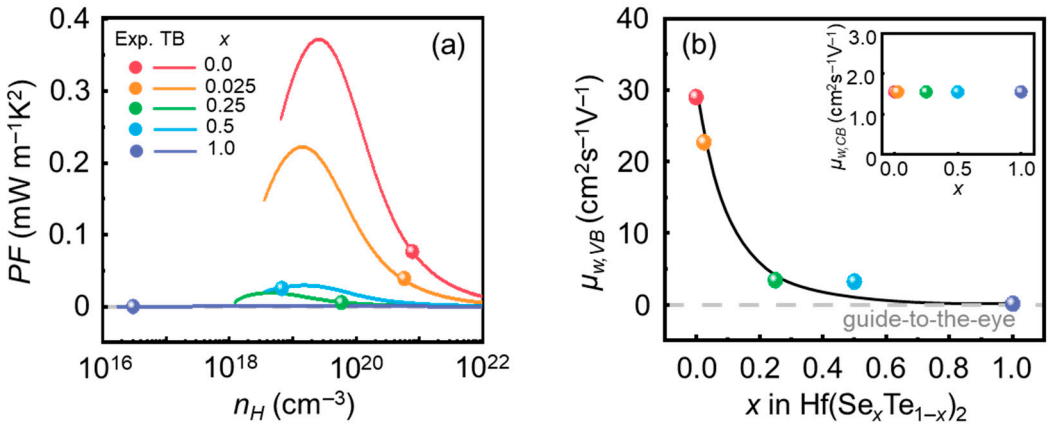

Figure 3. (**a**) Experimental (symbols) and theoretical (lines) power factor (*PF*) in terms of n_H for $Hf(Te_{1-x}Se_x)_2$ (x = 0.0, 0.025, 0.25, 0.5, and 1.0) at 300 K [22], (**b**) estimated $\mu_{W,VB}$ (= μ_W for holes) in terms of Se alloying content (x) at 300 K. The x-dependent $\mu_{W,CB}$ (= μ_W for electrons) at 300 K is provided in the inset.

When there is only one band contributing to electronic transport, the theoretical maximum *PF* is directly proportional to the μ_W of the band. When there are two bands (valence and conduction bands) contributing, the theoretical maximum *PF* is related to the interplay between the $\mu_{W,maj}$ and $\mu_{W,min}$. Out of the two band parameter, $\mu_{W,maj}$ would be more important when determining the theoretical maximum *PF*. Figure 3b shows the $\mu_{W,VB}$ and $\mu_{W,CB}$ (inset) of $Hf(Te_{1-x}Se_x)_2$ (x = 0.0, 0.025, 0.25, 0.5, and 1.0) at 300 K. Because we assume that the $m_{d,CB}$* and $\mu_{0,CB}$ are invariant with x, corresponding $\mu_{W,CB}$ (Equation (13)) in terms of x (Figure 3b inset) is also independent to x. Generally, the calculated $\mu_{W,VB}$ decreases with increasing x. The values of $\mu_{W,VB}$ are approximately proportional to the theoretical maximum *PF* in Figure 3a. The values of $\mu_{W,VB}$ are not directly proportional to the theoretical maximum *PF* as the $\mu_{W,CB}$ values also contribute when determining the theoretical maximum *PF*. The contribution from $\mu_{W,CB}$ becomes larger for small x as the ε_g reduces for decreasing x (Table 1).

3.4. Estimation of the Bipolar Thermal Conductivity (κ_b) Via the TB Model

Figure 4a presents the theoretical weighted mobility ratio a computed using the $\mu_{W,VB}$ and $\mu_{W,CB}$ from Figure 3b. The A is defined as the ratio of $\mu_{W,maj}$ to $\mu_{W,min}$ (Equation (14)). Because $Hf(Te_{1-x}Se_x)_2$ (x = 0.0, 0.025, 0.25, 0.5, and 1.0) alloys are p-type, the A in Figure 4a is obtained by $\mu_{W,VB}$ divided by $\mu_{W,CB}$. As we have kept the $\mu_{W,CB}$ constant for all x, the trend calculated in the A is almost identical to that observed in $\mu_{W,VB}$. Similar to the $\mu_{W,VB}$, the A rapidly decreases with increasing x. Except x = 0.0 and 0.025, the A of all x are smaller than 2.2. What A represents is how mobile majority carriers are with respect to the minority carriers. If A is much larger than one, it means that the majority carriers move much faster than minority carriers. In such a case, the bipolar contribution to electronic contribution weakens. Therefore, a much-suppressed bipolar conduction is expected when the A is large. According to Figure 4a, the samples with small x would experience much weaker bipolar conduction than those with large x. However, this only applies when other factors that affect the κ_b stay the same.

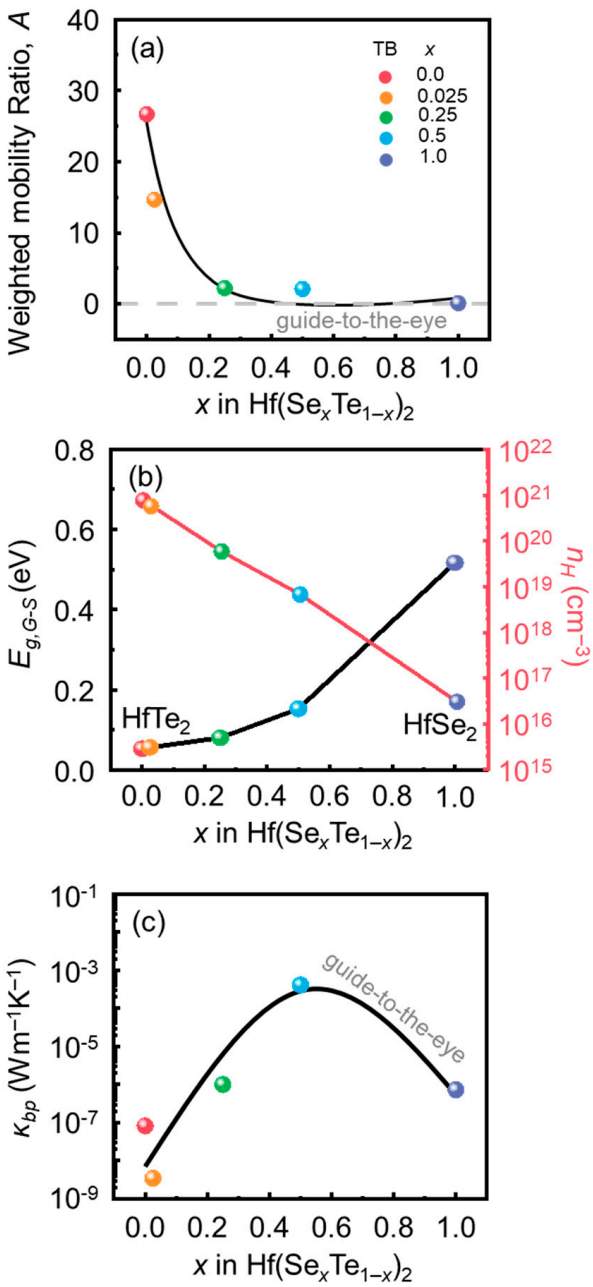

Figure 4. (**a**) Theoretical (symbols)-weighted mobility ratio a in terms of x for $Hf(Te_{1-x}Se_x)_2$ (x = 0.0, 0.025, 0.25, 0.5, and 1.0) at 300 K, (**b**) experimental (symbols) band gap estimated via Goldsmid–Sharp equation ($E_{g,G\text{-}S}$), and experimental (symbols) n_H in terms of x at 300 K [22], (**c**) theoretical (symbols) bipolar thermal conductivity (κ_b) estimated for different x via the TB model at 300 K.

Figure 4b shows how the band gap estimated using the Goldsmid–Sharp equation ($E_{g,G\text{-}S}$) and the measured n_H change in terms of x. The band gap and n_H are also important factors that affect the κ_b. First of all, increasing the band gap will decrease the κ_b. Secondly, increasing n_H will also decrease the κ_b. In $Hf(Te_{1-x}Se_x)_2$ (x = 0.0, 0.025, 0.25, 0.5, and 1.0) alloys, increasing x will increase $E_{g,G\text{-}S}$ but decrease the n_H at the same time. From Figure 4a,b, we now know that the increasing x will decrease A and n_H, but increase $E_{g,G\text{-}S}$. We have two factors (A and n_H) changing to increase the κ_b, and one factor ($E_{g,G\text{-}S}$) changing to suppress the κ_b with increasing x. The relative impact of each factor on κ_b is difficult to evaluate as those factors are strongly interdependent. Instead, the κ_b itself is estimated to see which factor affects bipolar conduction more strongly.

Figure 4c is the κ_b in terms of x estimated by using the TB model at 300 K. The κ_b is a function of S_i, σ_i (i = *maj*, *min*), and T (Equation (16)). The S_i and σ_i (i = *maj*, *min*) are defined as in Equations (2)–(3) and (5)–(6) [26–33].

$$\kappa_b = \left[\sigma_{maj}S_{maj}^2 + \sigma_{min}S_{min}^2 - \frac{\left(\sigma_{maj}S_{maj} + \sigma_{min}S_{min}\right)^2}{\sigma_{maj} + \sigma_{min}}\right]T \quad (16)$$

According to Figure 4c, the κ_b increases with x until x = 0.5, and for x > 0.5 it starts to decrease. For small x, the $E_{g,G\text{-}S}$ is also narrow. In such a circumstance, decreases in A and n_H result in an increase in κ_b. However, once the $E_{g,G\text{-}S}$ becomes wider than 0.15 eV (when x = 0.5), the effect of the band gap on bipolar conduction becomes much greater than those of A and n_H. Hence, despite the decrease in A and n_H, a reduction in κ_b is obtained with the band gap increase.

4. Conclusions

In summary, the electronic transport properties of p-type $Hf(Te_{1-x}Se_x)_2$ (x = 0.0, 0.025, 0.25, 0.5, and 1.0) alloys have been investigated in terms of electronic band parameters. Because the band gap of the $Hf(Te_{1-x}Se_x)_2$ alloys increases with increasing x, the Two-Band (TB) model (one valence band and one conduction band) has been adopted to take the band gap change into consideration. When we consider the majority carrier band (valence band in this case), its density-of-states effective mass first decreases but for x > 0.25, it increases again. The deformation potential increases with increasing x. Consequently, the weighted mobility and weighted mobility ratio of the valence band decrease with increasing x. The bipolar thermal conductivity is also estimated using the TB model. It peaks near x = 0.5 and decreases for x > 0.5. This trend observed in the bipolar thermal conductivity can be explained with the weighted mobility ratio, band gap, and carrier concentration change with increasing x. When the band gap is narrow (x < 0.5), the effects of the weighted mobility ratio and carrier concentration are strong, but when the band gap becomes wide (x > 0.5), the band gap becomes a more critical factor to bipolar conduction than the other two factors.

Author Contributions: Data curation, J.-Y.K.; Writing—original draft, S.-M.H. and S.-i.K.; Writing—review & editing, H.-S.K.; Visualization, M.H.; Supervision, H.-S.K. All authors have read and agreed to the published version of the manuscript.

Funding: This work was financially supported by the National Research Foundation of Korea (NRF), funded by the Ministry of Education (NRF-2021K2A9A1A06092290).

Institutional Review Board Statement: Not applicable.

Informed Consent Statement: Not applicable.

Data Availability Statement: The data presented in this study are available on request from the corresponding author.

Conflicts of Interest: The authors declare no conflict of interest.

References

1. Petsagkourakis, I.; Tybrandt, K.; Crispin, X.; Ohkubo, I.; Satoh, N.; Mori, T. Thermoelectric materials and applications for energy harvesting power generation. *Sci. Technol. Adv. Mater.* **2018**, *19*, 836–862. [CrossRef]
2. Tritt, T.M.; Subramanian, M.A. Thermoelectric Materials, Phenomena, and Applications: A Bird's Eye View. *MRS Bull.* **2006**, *31*, 188–198. [CrossRef]
3. Caballero-Calero, O.; Ares, J.R.; Martín-González, M. Environmentally Friendly Thermoelectric Materials: High Performance from Inorganic Components with Low Toxicity and Abundance in the Earth. *Adv. Sustain. Syst.* **2021**, *5*, 2100095. [CrossRef]
4. Rosi, F.D. Thermoelectricity and thermoelectric power generation. *Solid State Electron.* **1968**, *11*, 833–868. [CrossRef]
5. Liu, W.; Jie, Q.; Kim, H.S.; Ren, Z. Current progress and future challenges in thermoelectric power generation: From materials to devices. *Acta Mater.* **2015**, *87*, 357–376. [CrossRef]
6. Snyder, G.J.; Toberer, E.S. Complex thermoelectric materials. *Nat. Mater.* **2008**, *7*, 105–114. [CrossRef]

7. Lee, K.H.; Kim, Y.M.; Park, C.O.; Shin, W.H.; Kim, S.W.; Kim, H.S.; Kim, S.i. Cumulative defect structures for experimentally attainable low thermal conductivity in thermoelectric $(Bi,Sb)_2Te_3$ alloys. *Mater. Today Energy* **2021**, *21*, 100795. [CrossRef]
8. Feng, Y.; Li, J.; Li, Y.; Ding, T.; Zhang, C.; Hu, L.; Liu, F.; Ao, W.; Zhang, C. Band convergence and carrier-density fine-tuning as the electronic origin of high-average thermoelectric performance in Pb-doped GeTe-based alloys. *J. Mater. Chem. A* **2020**, *8*, 11370–11380. [CrossRef]
9. Kim, H.-S.; Heinz, N.A.; Gibbs, Z.M.; Tang, Y.; Kang, S.D.; Snyder, G.J. High thermoelectric performance in (Bi0.25Sb0.75)2Te3 due to band convergence and improved by carrier concentration control. *Mater. Today* **2017**, *20*, 452–459. [CrossRef]
10. Hong, T.; Wang, D.; Qin, B.; Zhang, X.; Chen, Y.; Gao, X.; Zhao, L.-D. Band convergence and nanostructure modulations lead to high thermoelectric performance in SnPb0.04Te-y% AgSbTe2. *Mater. Today Phys.* **2021**, *21*, 100505. [CrossRef]
11. Moshwan, R.; Liu, W.-D.; Shi, X.-L.; Wang, Y.-P.; Zou, J.; Chen, Z.-G. Realizing high thermoelectric properties of SnTe via synergistic band engineering and structure engineering. *Nano Energy* **2019**, *65*, 104056. [CrossRef]
12. Wang, N.; Li, M.; Xiao, H.; Gao, Z.; Liu, Z.; Zu, X.; Li, S.; Qiao, L. Band degeneracy enhanced thermoelectric performance in layered oxyselenides by first-principles calculations. *Npj Comput. Mater.* **2021**, *7*, 18. [CrossRef]
13. Dangić, Đ.; Hellman, O.; Fahy, S.; Savić, I. The origin of the lattice thermal conductivity enhancement at the ferroelectric phase transition in GeTe. *Npj Comput. Mater.* **2021**, *7*, 57. [CrossRef]
14. Chhowalla, M.; Shin, H.S.; Eda, G.; Li, L.-J.; Loh, K.P.; Zhang, H. The chemistry of two-dimensional layered transition metal dichalcogenide nanosheets. *Nat. Chem.* **2013**, *5*, 263–275. [CrossRef] [PubMed]
15. Muratore, C.; Varshney, V.; Gengler, J.J.; Hu, J.J.; Bultman, J.E.; Smith, T.M.; Shamberger, P.J.; Qiu, B.; Ruan, X.; Roy, A.K.; et al. Cross-plane thermal properties of transition metal dichalcogenides. *Appl. Phys. Lett.* **2013**, *102*, 081604. [CrossRef]
16. Isomäki, H.; Boehm, J.v. Bonding and Band Structure of ZrS_2 and $ZrSe_2$. *Phys. Scr.* **1981**, *24*, 465. [CrossRef]
17. Gaiser, C.; Zandt, T.; Krapf, A.; Serverin, R.; Janowitz, C.; Manzke, R. Band-gap engineering with HfS_xSe_{2-x}. *Phys. Rev. B* **2004**, *69*, 075205. [CrossRef]
18. Bilc, D.I.; Benea, D.; Pop, V.; Ghosez, P.; Verstraete, J. Electronic and Thermoelectric Properties of Transition-Metal Dichalcogenides. *J. Phys. Chem. C B* **2021**, *125*, 27084–27097. [CrossRef]
19. Ge, Y.; Wan, W.; Ren, Y.; Liu, Y. Large thermoelectric power factor of high-mobility transition-metal dichalcogenides with $1T''$ phase. *Phys. Rev. Res.* **2020**, *2*, 013134. [CrossRef]
20. Bharadwaj, S.; Ramasubramaniam, A.; Ram-Mohan, L.R. Lateral transition-metal dichalcogenide heterostructures for high efficiency thermoelectric devices. *Nanoscale* **2022**, *14*, 11750–11759. [CrossRef]
21. Yumnam, G.; Pandey, T.; Singh, A.K. High temperature thermoelectric properties of Zr and Hf based transition metal dichalcogenides: A first principles study. *J. Chem. Phys.* **2015**, *143*, 234704. [CrossRef] [PubMed]
22. Bang, J.; Kim, H.-S.; Kim, D.H.; Lee, S.W.; Park, O.; Kim, S.-I. Phase formation behavior and electronic transport properties of HfSe2-HfTe2 solid solution system. *J. Alloys Compd.* **2022**, *920*, 166028. [CrossRef]
23. May, A.F.; Snyder, G.J. Introduction to Modeling Thermoelectric Transport at High Temperatures. In *Materials, Preparation, and Characterization in Thermoelectrics*; CRC Press: Boca Raton, FL, USA, 2012; pp. 1–18.
24. Goldsmid, H.J.; Sharp, J.W. Estimation of the thermal band gap of a semiconductor from seebeck measurements. *J. Electron. Mater.* **1999**, *28*, 869–872. [CrossRef]
25. Gibbs, Z.M.; Kim, H.-S.; Wang, H.; Snyder, G.J. Band gap estimation from temperature dependent Seebeck measurement—Deviations from the $2e|S|_{max}T_{max}$ relation. *Appl. Phys. Lett.* **2015**, *106*, 022112. [CrossRef]
26. Foster, S.; Neophytou, N. Effectiveness of nanoinclusions for reducing bipolar effects in thermoelectric materials. *Com. Mat. Sci.* **2019**, *164*, 91–98. [CrossRef]
27. Graziosi, P.; Neophytou, N. Bipolar conduction asymmetries lead to ultra-high thermoelectric power factor. *Appl. Phys. Lett.* **2022**, *120*, 072102. [CrossRef]
28. Hong, M.; Chen, Z.-G.; Yang, L.; Zou, J. Enhancing thermoelectric performance of Bi_2Te_3-based nanostructures through rational structure design. *Nanoscle* **2016**, *8*, 8681–8686. [CrossRef]
29. Bahk, J.-H.; Shakouri, A. Enhancing the thermoelectric figure of merit through the reduction of bipolar thermal conductivity with heterostructure barriers. *Appl. Phys. Lett.* **2014**, *105*, 052106. [CrossRef]
30. Burke, P.G.; Curtin, B.M.; Bowers, J.E.; Gossard, A.C. Minority carrier barrier heterojunctions for improved thermoelectric efficiency. *Nano Energy* **2015**, *12*, 735–741. [CrossRef]
31. Muzaffar, M.U.; Zhu, B.; Yang, Q.; Zhou, Y.; Zhang, S.; Zhang, Z.; He, J. Suppressing bipolar effect to broadening the optimum range of thermoelectric performance for p-type bismuth telluride–based alloys via calcium doping. *Mater. Today Phys.* **2019**, *9*, 100130. [CrossRef]
32. Parker, D.; Singh, D.J. Thermoelectric properties of $AgGaTe_2$ and related chalcopyrite structure materials. *Phys. Rev. B* **2012**, *85*, 125209. [CrossRef]
33. Zhang, L.; Xiao, P.; Shi, L.; Henkelman, G.; Goodenough, J.B.; Zhou, J. Suppressing the bipolar contribution to the thermoelectric properties of $Mg_2Si_{0.4}Sn_{0.6}$ by Ge substitution. *J. Appl. Phys.* **2015**, *117*, 155103. [CrossRef]